**This document is downloaded from DR-NTU (https://dr.ntu.edu.sg)**
**Nanyang Technological University, Singapore.**

# Structural behavior of RC beam-column subassemblages under a middle column removal scenario

Yu, Jun; Tan, Kang Hai

2013

Yu, J., & Tan, K. H. (2013). Structural Behavior of RC Beam-Column Subassemblages under a Middle Column Removal Scenario. Journal of Structural Engineering, 139(2), 233-250.

https://hdl.handle.net/10356/98138

https://doi.org/10.1061/(ASCE)ST.1943-541X.0000658

© 2013 ASCE. This is the author created version of a work that has been peer reviewed and accepted for publication by Journal of structural engineering, ASCE. It incorporates referee’ s comments but changes resulting from the publishing process, such as copyediting, structural formatting, may not be reflected in this document. The published version is available at: [DOI:http://dx.doi.org/10.1061/(ASCE)ST.1943-541X.0000658].

*Downloaded on 25 Aug 2022 18:30:52 SGT*

Structural behavior of reinforced concrete beam-column sub-assemblages under a middle column removal scenario

Jun Yu [1], and Kang Hai Tan [2]

**Abstract**

Six reinforced concrete (RC) beam column sub-assemblages, consisting of two single-bay beams, one middle joint and two end column stubs, were quasi-statically tested under a middle column removal scenario. The tests were aimed to investigate if there are alternate load paths that can mitigate progressive collapse. With adequate axial restraints, both compressive arch action (CAA) and catenary action could be mobilized, significantly increasing the structural resistance beyond the beam flexural capacity. The effects of the top and bottom reinforcement ratios at the joint interfaces and beam span-to-depth ratio on structural behavior were studied. Results show that CAA is more beneficial to the sub-assemblages with a short span-to-depth ratio and a low reinforcement ratio, whereas catenary action is more favorable to the sub-assemblages with a large span-to-depth ratio and a high reinforcement ratio, particularly the top reinforcement ratio. As the last defense mechanism to prevent structural collapse, the development of catenary action is highlighted. The onset of catenary action corresponds to the transition of beam axial force from compression to tension, typically occurring at a central deflection around one beam depth in the tests if no shear failure precedes catenary action. At catenary action stage, prior to fracture of bottom bars, structural resistance is contributed by both beam axial tension from longitudinal reinforcement and shear force due to dowel action. If the contribution from rising axial tension exceeds the loss due to declining shear force, structural resistance will still keep on increasing until the fracture of top bars. Finally, the authors suggest a deformation criterion to determine

[1] Ph. D. Student, School of Civil & Environmental Engineering, Nanyang Technological University, 50 Nanyang Avenue, Singapore. Email: yuju0001@e.ntu.edu.sg, Tel: +65-67906199; fax: +65-67916697.
[2] Professor, School of Civil & Environmental Engineering, Nanyang Technological University, 50 Nanyang Avenue, Singapore.

catenary action of RC sub-assemblages, i.e. when the deflection at the middle joint attains 10% of the total beam span length, catenary action capacity is reached. The conservatism of this criterion for design purpose is also discussed.

**Keywords**: reinforced concrete, beam-column sub-assemblages, progressive collapse, alternate load path, compressive arch action, catenary action

## Introduction

With the threat of terrorist attacks looming large, the ability of a building to mitigate progressive collapse is of key interest to government agencies. To facilitate design, both indirect and direct methods have been proposed in current building codes (ASCE 2005; CEN 1991-2-7 2006) and design guidelines (DoD 2010; GSA 2003). The indirect method specifies a minimum level of connectivity among various structural components, and no structural analysis is required. The direct method falls into two general categories (Ellingwood and Leyendecker 1978): (1) *Specific local resistance method* and (2) *Alternate load path (ALP) method*. The former seeks to provide sufficient strength to resist failure from a specific threat. The latter (i.e. ALP method) allows local failure to occur, but seeks to provide ALPs so that damage is absorbed and major collapse is averted. The ALP approach forms the first proposal of a quantifiable model for designing robust buildings (Gurley 2008). The structural analysis via ALP requires notional removal of any one column or bearing wall, etc. Accordingly, the research and design interest is in the structural behavior after a column has been forcibly removed.

For RC frames, typical ALPs include flexural action (or virendeel action), compressive arch action (CAA) and catenary action, in which flexural action is based on pure flexural resistance of RC members. However, both CAA and catenary action require the development of axial force along a beam, in which the former needs compression and the latter tension (Su et al. 2009; Yu and Tan 2011). Moreover, catenary action in beams is regarded as the last defense mechanism to prevent structural collapse, since it always involves large deformations and utilizes tensile force to balance gravity loads. With increasing RC beam deflection, typically flexural action, CAA and catenary action will be sequentially mobilized. At least, a structure with normal design can attain the flexural capacity to mitigate progressive collapse since flexural action requires the smallest beam deflection among three different structural mechanisms. However, CAA and catenary action are beyond conventional design, and whether they can fully develop depends on many

factors, including geometrical and material properties of structures, and lateral restraints from surrounding structures, etc. In this paper, the scenario is restricted to the removal of a middle column of a multi-bay frame, so that lateral restraints are assumed to be adequate to allow the development of CAA and catenary action in the affected sub-assemblage.

By analogous to "compressive membrane action" of RC slabs (Park and Gamble 2000), the terminology of "compressive arch action" is used to emphasize the effect of beam axial compression on structural resistance, rather than to indicate that the structural mechanism is pure arch action. Several research publications (Sasani et al. 2011; Su et al. 2009; Yu and Tan 2010b; 2011) have pointed out that the presence of beam axial compression enhances the flexural strength of a beam via standard flexural-axial interaction and in turn its resistance to progressive collapse. Moreover, the mobilization of CAA depends on the boundary conditions of beams, which are provided by the remaining structure. Therefore, CAA can be categorized as a frame action. Similarly, Virendeel action (Sasani et al. 2007) is also one of frame actions, but it relies on double-curvature-shaped deformations of beams and columns without axial compression. To be more specific, the terminology of "compressive arch action" is adopted to describe the structural mechanism of sub-assemblages associated with beam axial compression in this paper.

Currently, only a few experimental programs have been conducted to deepen the understanding of structural behavior of RC structures under a middle column removal scenario (Orton et al. 2009; Sasani and Kropelnicki 2008; Su et al. 2009; Yi et al. 2008; Yu and Tan 2011). However, the study is at its infancy stage with very limited information of the effects of different parameters on structural behavior of beam-column sub-assemblages. This paper presents an experimental program and results of six RC beam-column sub-assemblages, which were designed in accordance with ACI 318-05 (American Concrete Institute 2005), to investigate the influences of different design parameters on structural behavior. Variations of structural behavior and load transfer mechanisms are comprehensively illustrated at structural level (relationships of applied

load and horizontal reaction force to middle joint displacement), cross-sectional level (variations of internal forces at a section) and fiber level (distribution of longitudinal reinforcement strains).

## Experimental program

After two preliminary tests were conducted on RC beam-column sub-assemblages (Yu and Tan 2010a; 2011), another six specimens were tested with an improved test set-up to investigate the effects of 1) reinforcement ratio through joints, 2) reinforcement detailing at joint regions, and 3) beam span-to-depth ratio on structural behavior of RC sub-assemblages, under a middle column removal scenario. Note that this program aims to study the structural behavior of directly affected sub-assemblages after the middle column has been removed and it is immaterial how this comes about.

### *Specimen design*

Six one-half scaled RC beam-column sub-assemblages were designed based on the detailing of specimens S1 and S2 (Yu and Tan 2011), consisting of two single-bay beams, a middle joint and two enlarged column stubs at the beam ends. The geometrical properties and the detailing of specimens are listed in Fig. 1 and Table 1. Due to symmetry, only half of a specimen is shown in Fig. 1. In the notations of sub-assemblages listed in Table 1, the first and the second numerals after a dash stand for the percentage of top and bottom reinforcement in the middle joint regions, respectively, and the third numeral denotes the beam span-to-depth ratio. For example, S4-1.24/0.82/23 indicates that S4 was designed with a top reinforcement ratio of 1.24% and a bottom reinforcement ratio of 0.82% at the joint regions and a beam span-to-depth ratio of 23.

S1 and S2 were designed in accordance with ACI 318-05 with seismic and non-seismic detailing, respectively (Yu and Tan 2011). Specimens S3 to S6 remained the same geometric dimensions as S1 and S2, but had different longitudinal reinforcement. Variations of top reinforcement ratios at A-A section and bottom reinforcement ratios at B-B sections as shown in Fig. 1 are within a

range corresponding to a tension-controlled flexural failure of beams initiated by yield of the steel reinforcement. According to the integrity of reinforcement provisions specified by ACI 318-05, at least two continuous bars should be respectively provided at both the top and the bottom of perimeter beams, as shown in Table 1. After a middle column is removed, due to a reversal of the bending moment near the middle joint under gravity loads, the top and bottom reinforcement ratios at the middle joint interfaces become critical parameters. As a result, specimens S3, S4 and S5 were used to investigate the effect of bottom reinforcement ratio at the middle joint interfaces on structural behavior, with the respective ratio of 0.49%, 0.82% and 1.24%. Specimens S4 and S6 were used to investigate the effect of top reinforcement ratio on structural behavior, with the ratio of 1.24% and 1.87%, respectively. Su et al. (2009) pointed out that beam span-to-depth ratio is a critical parameter that affects structural behavior under a middle column removal scenario, in particular for CAA. Therefore, specimens S4, S7 and S8 were used to study the effect of beam span-to-depth ratio on structural behavior, in which S7 and S8 remained the same beam sections and longitudinal reinforcement ratios as S4 but had different beam net-spans.

The curtailments of top and bottom reinforcement were determined according to ACI detailing manual-2004 (American Concrete Institute 2004). The tests on specimens S1 and S2 (Yu and Tan 2011) indicated that the arrangement of beam stirrups (according to seismic detailing) did not affect the structural behavior of RC sub-assemblages under such a scenario. Therefore, the beam stirrups for specimens S3 to S8 were kept constant (R6@100 mm), as shown in Fig. 1. The tests on S1 and S2 also showed that the lap-splice of bottom reinforcement at the middle joint, with Class A splice according to ACI 318-05, satisfied the requirements on continuity of longitudinal reinforcement, and the lap-splice did not affect overall behavior except local failures, such as cracks, pullout and fracture of reinforcing bars near the middle joint interfaces. These local failures could be used to study the effect of detailing on load transfer mechanisms within joints. Therefore, in specimens S3 and S6, lap-splice of bottom bars was employed.

*Material properties*

Material tests were conducted according to ASTM specifications to obtain the representative strengths of steel reinforcement and concrete. For each type of steel reinforcement, three specimens were used for tensile tests, and the corresponding material properties are included in Table 2. Representative stress-strain relationships of different reinforcing bars are shown in Fig. 2. The stress of a bar was determined based on the nominal cross-sectional area. For concrete, six cylinders with 150 mm diameter and 300 mm height were used for compressive tests and three cylinders with the same dimensions for split-cylinder tests. The compressive strength of concrete is 38.2 MPa, the tensile strength is 3.5 MPa, and the initial modulus of elasticity is 29.6 GPa.

*Test set-up*

The boundary conditions of the sub-assemblage specimens shown in Fig. 1 were achieved by the test set-up demonstrated in Fig. 3. The ends of each specimen were respectively connected to a reaction wall and a steel A-frame via two horizontal pin-pin connections. A load cell was installed in each horizontal connection to measure the corresponding horizontal reaction force. In the vertical direction, each end of the specimens was supported by a pin support seated onto three steel rollers, which were used to eliminate the effect of horizontal forces on vertical support reaction forces. Moreover, compression load cells were installed between the ground and the steel plate that used to place steel rollers. Therefore, the measurements of vertical and horizontal reaction forces were independent of each other. A concentrated load was then applied at the top of a middle joint through a hydraulic actuator reacted against a steel portal frame. To prevent out-of-plane movement of slender specimens, two out-of-plane restraints were installed at both sides of the middle joint. Detailed information on the similar test set-up can also be found in the paper (Yu and Tan 2011). During the testing, the load was imposed with displacement control at a rate of 0.1 mm/sec until a specimen completely failed. This quasi-static loading neglects the dynamic nature of progressive collapse. However, with the incorporation of dynamic increase factors as

recommended by the design guideline UFC 4-023-3 (DoD, 2010), nonlinear static behavior can be used for evaluation of progressive collapse resistance.

The tests on specimens S1 and S2 (Yu and Tan 2011) showed that once the cracks at one side of the middle joint was more developed than the other side due to non-uniformity of material and imperfection of cast geometry, cracks in the subsequent loading process would be concentrated at the weaker side. Due to the lack of a rotational restraint at the middle joint, inevitably, the joint tended to rotate towards the more severely cracked side. The test on a multi-story frame (Yi et al. 2008) showed that the rotation of the middle joint was restrained by the column connected to the upper story. Therefore, a rotational restraint at the middle joint was installed in the test rig. As highlighted in Fig. 3, two steel shafts, going through precast holes in the middle joint, were located in the gap of two steel columns. During the initial loading process, two shafts could move freely along the gap without touching the flanges of the upright steel columns. However, when bottom reinforcing bars were fractured or pulled out at one joint side, the shafts would come into contact with steel column flanges, giving rise to a force couple which acted against the rotation of the middle joint. After the bottom bars at both sides of the middle joint were fractured or pulled out, the force transfer at both joint interfaces were quite symmetrical and the rotational restraint did not provide any force couple. Friction in vertical direction was generated when the shafts came into contact with column flanges. However, since lubricant was applied on the surfaces of the steel column flanges and the vertical reaction forces were measured, the influence of friction on the applied load could be eliminated.

*Instrumentation*

All reaction forces at each side, indicated as $V_1$, $H_1$ and $H_2$ in Fig. 4, were independently measured by respective load cells, and the applied load was measured by an in-built load cell of the actuator. Therefore, the whole test rig was a statically-determinate system. The displacements at the middle joint and along the beam were measured via line displacement transducers (LDTs)

and linear variable differential transformers (LVDTs), as shown in Fig. 4. Consequently, the beam deflection curve at each load step could be determined, and the cross-sectional forces at a section including axial force, bending moment and shear force, could be computed for each deformed configuration. Additionally, the movements at the specimen ends were measured to ascertain restraint stiffnesses. To obtain the variations of reinforcement strain under different structural mechanisms, strain gages were attached onto the surface of reinforcement prior to casting.

**Experimental results**

Testing was stopped when the top bars near either end column stub interface of each specimen completely severed. Based on detailed instrumentation, the results are demonstrated at structural, sectional and fiber levels. At structural levels, the relationships of applied loads and horizontal reactions vs. middle joint displacement (MJD) are used to represent the overall behavior, as shown in Figs. 5-7. The effect of the rotational restraint on the horizontal reaction forces at both sides of a specimen is illustrated in Fig. 8. In addition, global and local failure modes of specimens are demonstrated in Figs. 9-12. Finally, the overall deflection curves of a specimen and the development of local rotations are shown in Figs. 13 and 14.

At sectional level, the determination and variations of cross-sectional forces, including bending moment, axial force and shear force, are demonstrated in Figs. 15-17. The variations of cross-sectional forces can be further used to illustrate the force transfer mechanism at catenary action stage. At fiber level, the strain variations of longitudinal reinforcing bars and stirrups elucidate the force transfer over the bars at different structural mechanisms, as shown in Figs. 18 and 19.

*Applied load and horizontal reaction vs. middle joint displacement*

Figs. 5(a)-7(a) show the load-MJD relationships of all specimens. The sudden reductions marked by a cross resulted from bottom bar fracture near the middle joint interfaces, and the other sudden reductions were caused by top bar fracture near the end column stub interfaces.

Figs. 5(b)-7(b) show the horizontal reaction force-MJD relationships of all specimens. The horizontal reaction at each end of a specimen is the sum of reactions of two horizontal restraints, as shown in Fig. 2. Figs. 8(a) and (b) show the development of horizontal reaction at each end of specimens S4 and S5, respectively. It can be found that between the sequential fractures of bottom bars near the middle joint interfaces, the horizontal reactions at both ends of a specimen were not equal due to the horizontal forces provided by the rotational restraint at the middle joint. Other than this range, the measurement shows good agreement of horizontal reactions at two ends, indicating that the rotational restraint only functioned to restrain the joint rotation between the sequential fractures of bottom bars. Accordingly, the average values of the horizontal reactions are used in Figs. 5(b)-7(b). It will be shown later that the beam axial force-MJD relationship is almost the same as the horizontal reaction-MJD relationship. Therefore, Figs. 5(b)-7(b) can also represent the variations of beam axial forces. The positive and negative values denote beam axial tension and compression, respectively.

Figs. 5(b)-7(b) indicate that the beam axial compression was induced at very small vertical displacements. As a result, there is no pure flexural action and no distinct demarcation between flexural action and CAA. However, pure flexural capacity, namely $P_f$, is widely used in design codes to evaluate the ultimate capacity of RC members. Therefore, it can be used as a baseline of structural resistance and is set as a hypothetical demarcation of flexural action and CAA. $P_f$ is calculated by a mechanism that plastic hinges occur at two joint interfaces and at two end column stub interfaces without considering the presence of beam axial force. Table 3 summarizes $P_f$, the

first peak load $P_{caa}$, i.e. CAA capacity, and maximum axial compression $N_{max}$ for all specimens. It can be seen that $P_{caa}$ exceeds $P_f$ for all specimens. The enhancement of structural resistance at CAA stage is mainly ascribed to the presence of beam axial compression, which enhances the corresponding ultimate moment of resistance of a section. After $P_{caa}$, due to second-order effect and concrete crushing near the joint and end column stub interfaces, the applied load decreased with increasing MJD.

With further increasing MJD, when the beam axial force changed from compression to tension, catenary action kicked in. This is because the essence of catenary action is a tensile mechanism. After this transition point, applied loads increased again until bar fracture. Out of brevity, three different structural mechanisms of specimen S4 are denoted in Fig. 6, and the categorization of structural mechanisms for the other specimens is broadly similar. Table 4 lists the detailed information at catenary action stage, including the MJD corresponding to the onset of catenary action, the load and corresponding MJD at each bar fracture. It can be seen that except S8, catenary action capacities of specimens S3 to S7 are greater than their CAA capacities.

*Effect of bottom reinforcement ratio (BRR) at joints on structural behavior*

Fig. 5 shows the effect of BRR at the middle joint on the overall structural behavior of sub-assemblages. The top reinforcement ratios (TRR) for the three specimens are the same, i.e. at 1.24%. Within CAA and the initial stage of catenary action prior to bottom bar fracture, a higher BRR gives rise to a higher structural resistance for the same deflection. In other words, if a structure is expected to provide a larger resistance against progressive collapse at a relatively smaller displacement, more bottom reinforcement is required. In this sense, seismic detailing is beneficial to increase progressive collapse resistance, as the bottom reinforcement should not be less than half of the top reinforcement in a joint (ACI 318-05). For specimen S5 with BRR equal to TRR, prior to the first fracture of bottom bars, catenary action has attained the resistance of

94.86 kN, around 35% larger than the CAA capacity $P_{caa}$ of 70.33 kN. However, for specimens S3 and S4, at the first fracture of bottom bars, the structural resistance due to catenary action did not exceed the CAA capacity. Fig. 5 also shows that a greater BRR can delay the first fracture of bottom bars. Table 3 shows that for specimens S4, S5 and S6, a higher BRR results in a lower enhancement factor due to CAA.

*Effect of top reinforcement ratio (TRR) at joints on structural behavior*

Fig. 6 shows the effect of TRR at the middle joint on overall structural behavior of sub-assemblages. The BRRs for both specimens S4 and S6 are the same, i.e. at 0.82%. Due to the lap splice of bottom bars within the middle joint in specimen S6, two wide cracks were initiated at the free ends of splice bars when the MJD was small. Consequently, the stiffness of S6 was smaller than that of S4 before the capacity of CAA was attained, although TRR of S6 was larger than that of S4. A comparison of S4 and S6 in Fig. 6 indicates that the TRR is very beneficial to the overall structural behavior, since a greater TRR can provide a higher capacity of CAA, a higher resistance at the first fracture of bottom bars, and a much higher capacity of catenary action. The capacity of catenary action for specimen S6 is 143.28 kN, around 38% higher than that of S4. On the other hand, Table 3 shows that for S4 and S6, a higher TRR results in a lower enhancement factor due to CAA.

After a MJD of 530 mm, all the bottom bars for specimens S3, S4 and S5 had fractured, and the vertical load was sustained by the top bars only. As a result, the same top bars provided similar beam axial tension and structural resistance under the same MJD, as shown in Figs. 5(a) and (b), respectively. S3 achieved the largest capacity of catenary action at the expense of the largest MJD. This is because a larger MJD increases the vertical component of beam axial tension in resisting vertical loads. Therefore, TRR determines the capacity of catenary action for a given limit of MJD.

*Effect of beam span-to-depth ratio on structural behavior*

Fig. 7 shows that the beam span-to-depth ratio ($L/h$) affects structural behavior fundamentally, since catenary action did not significantly increase structural resistance of specimen S8 with the lowest $L/h$. The observed crack patterns of S8 indicate that shear behavior in specimen S8 was dominant, whereas specimens S4 and S7 were dominated by flexural and axial behavior. Despite 1.2 m shorter than the total span length of S4, S7 behaved similarly to S4. However, a further reduction of 1.2 m in the total span length (e.g. from S7 to S8) resulted in a completely different structural mechanism, suggesting that there is a threshold span-to-depth ratio that determines structural mechanism, such as catenary action. Fig. 7(b) demonstrates that the beam axial compression of specimen S8 was mobilized much more rapidly than S4 and S7 in the initial stage, and the beam axial force of S8 changed from compression to tension at a MJD of 136 mm, significantly smaller than that of the remaining two specimens, as shown in Fig. 7(b). However, the CAA capacity and the enhancement factor due to CAA of S8 are the largest amongst the six specimens. Therefore, RC beams with a short span-to-depth ratio are more likely to mitigate progressive collapse via CAA rather than catenary action.

The threshold span-to-depth ratio can be roughly estimated through a comparison of the CAA capacity and the maximum structural shear resistance. If the former is smaller than the latter, shear failure can be avoided and structural performance will be more ductile. For the given specimen detailing and the material properties as listed in Tables 1 and 2, respectively, the nominal sectional shear capacity $V_n$ is 75.69kN in accordance with ACI 318-05. If a strength reduction factor of 0.75 is considered, the shear design strength $\phi V_n$ is 56.77kN. Therefore, the structural resistance governed by shear is approximately between 113.54 kN and 151.38 kN. In this batch of specimens, only the CAA capacity of S8 exceeds 113.54 kN. As a result, shear failure occurred for S8, which can also confirmed by the crack pattern and the failure mode of S8.

*Failure modes and crack patterns of specimens S3 to S7*

Due to similar failure modes of specimens S3 to S7, for simplicity, specimen S5 is singled out to demonstrate the crack patterns and the failure modes. However, those of S8 are demonstrated separately due to its structural mechanism different from the other specimens.

Initially, S5 was mainly subjected to a coupled action of bending moment and beam axial compression. Fig. 9(a) shows that at the CAA capacity, there were only flexural cracks at the middle joint region and the beam ends, and the top concrete near the middle joint interface was crushed. When increasing MJD to greater than one beam depth, catenary action replaced CAA to sustain the vertical load with axial tension mobilized throughout the beam. Consequently, extensive tensile cracks, normal to the beam axis, were developed over the whole length, and some cracks even penetrated the entire beam cross-sections, as shown in Fig. 9(b). Two wide flexural cracks were concentrated at both joint interfaces, resulting in strain concentration and eventual fracture of bottom bars, as shown in Fig. 9(b). Due to the presence of the rotational restraint, the bottom bars at the other side of the middle joint were either fractured or pulled out. Thereafter, the tensile force could only be transferred via top bars going through the middle joint. When the top bars near one end column stub interface were completely fractured, as shown in Fig. 9(b), the whole sub-assemblage failed.

*Failure modes and crack patterns of specimen S8*

Similar to S5, severe failure of S8 was also concentrated at the middle joint region and the beam ends. Therefore, the crack patterns and the failure modes at these regions are demonstrated. Fig. 10(a) shows that when S8 was at CAA stage with a MJD of 75 mm, wide cracks occurred near the middle joint interface and inclined cracks appeared at the beam end, indicating large bending moments and shear forces, respectively. In fact, the shear forces caused fracture of two stirrups that were near the middle joint, as shown in Fig. 10(b). At catenary action stage, the shear cracks

and the flexural cracks intersected with each other, causing severe debonding of concrete. Moreover, shear failure inhibited a further large increase in structural resistance even though catenary action was mobilized.

*Summary of local failure modes at middle joints and beam ends*

Fig. 11 demonstrates local failure modes of regions near the middle joints. There was no appreciable shear distortion at the middle joint panels. All the failures were concentrated in the regions near the joint interfaces (or beam-column connections). For the specimens with *continuous bottom bars* (S4, S5, S7 and S8), two wide cracks just occurred at both joint interfaces, whereas for S3 and S6 with *lap-spliced bottom bars*, two wide cracks formed at the free ends of spliced bars. It can be observed that for S3, S6 and S7, the longitudinal bond cracks along the top bars ran perpendicular to and intersected with the flexural cracks, causing a loss of bond strength so that the stress along the top bars distributed more uniformly.

Fig. 12 shows that both flexural and shear cracks were extensively developed at the beam ends. Concrete at the compression side was crushed and spalled. The crack patterns reflect a coupled action of bending moment (or tension) and shear force. For specimens S6, S7 and S8, severe bond cracks are observed due to large tension. Figs. 5(b) to 7(b) show that the beam axial tension of specimen S6 was much larger than that of the other specimens at catenary action stage. Accordingly, more severe bond cracks occurred in S6.

*Overall deflections and local rotations of sub-assemblages*

Specimen S5 is selected to show overall deflections of sub-assemblages. The deflection curves shown in Fig. 13 at both sides of the middle joint are quite symmetrical until the first fracture of bottom bars. The position of bottom bar fracture was random, at either side of the middle joint. Fig. 13 shows that at catenary action stage, the slope of the deflection curves between the curtailment point of a top bar anchored into end column stubs and the middle joint interface is

larger than that of the beam end, since at the free end of the curtailed bars, cracks were more extensively developed due to large tension, as highlighted in Fig. 9(b).

The slope of the deflection curves in Fig. 13 represents the *local rigid rotation* $\theta_r$ of beam segments (such as AB, BC, CD, etc). Fig. 13 indicates that the distribution of $\theta_r$ is not uniform over the beam length. $\theta_r$ near the middle joint interface is larger than the one near the beam ends. On the other hand, in UFC 4-023-03 (DoD 2010), the rotation of an RC framed member is evaluated by *chord rotation*, $\theta_{cr}$, indicated as a dash straight line in Fig. 13. It implies that the entire single-bay beam rotates like a rigid body and the local rotation at each section is equal to $\theta_{cr}$. However, chord rotation $\theta_{cr}$ underestimates the local rotations near the joint interfaces but overestimates those at beam ends. The ultimate rotations at the end of tests are listed in Table 5. The wide cracks occurred at 50 mm and 100 mm away from joint interfaces for specimens S3 and S6, respectively, as shown in Figs. 11(a) and (d). Therefore, for S3 and S6, the local rigid rotation is specified at the position of the cracks rather than joint interfaces. It can be seen that the *local rotation capacities* at the joint interfaces and the beam ends are greater than 13.9° and 6.6°, respectively. In UFC 4-023-03 (DoD 2010), it is required that the *chord rotation capacity* of RC members should exceed 11.3° if catenary action is considered. Table 5 shows that the chord rotations capacities of all six specimens, each of which is calculated by the MJD just before complete fracture of top bars at one beam end, satisfy this requirement.

Fig. 14 shows the development of local rigid rotations $\theta_r$ of beam segments and chord rotation $\theta_{cr}$ in specimen S5. The notations of beam segments are indicated in Fig. 13. It is found that prior to fracture of bottom bars at one middle joint interface, $\theta_r$ of each beam segment was quite close to $\theta_{cr}$ expect for the segment A'B', which was adjacent to one middle joint interface. The $\theta_r$ of segment A'B' is underestimated because the rotation of the middle joint is not considered during

the calculation of $\theta_r$. After the 2nd fracture of bottom bars at the middle joint interface, the rotation of the middle joint was released. As a result, $\theta_r$ of segment A'B' became closer to the one of segment AB. In addition, after bottom bar fracture, local rotations were more concentrated near the middle joint so that local rigid rotations $\theta_r$ of segments AB, BC, A'B' and B'C' were greater than those of segments FG and F'G' (i.e. at beam ends).

*Variation of cross-sectional internal forces*

Fig. 15 shows the determination and sign conventions of cross-sectional forces at section *i*. All forces are calculated with reference to the geometric center of a section. Formulas in Fig. 15 indicate that except bending moment, both axial force and shear force at section *i* depend on rotation $\theta_i$. To evaluate cross-sectional forces accurately, local rotation $\theta_r$ should be used, as it accounts for the actual deformed configurations of beams. For convenience, chord rotation $\theta_{cr}$ can be used. However, the difference between $\theta_r$ and $\theta_{cr}$ may result in the discrepancies in predicting axial and shear forces.

The left one-bay beam of S5 as shown in Fig. 9 is used to demonstrate the relationships of cross-sectional forces to MJD. Fig. 16(a) shows variations of bending moments at the joint interface and the beam end. Both attained the respective maximum values when the beam axial compression reached the maximum, as shown Fig. 16(b), since axial compression increased the ultimate moment resistance via *M-N* interaction (Yu and Tan 2011). After the commencement of catenary action, the non-zero bending moments suggested that at catenary action stage, the reinforcing bars at critical sections were not in uniform tension. In other words, some bars were under larger tension and others were under smaller tension or even under compression. However, with the further development of catenary action, the bending moments kept decreasing, indicating that the distribution of tension over bars at one beam section tended to be uniform. After fracture of bottom bars, the joint interface was under pure tension of top bars. Nevertheless, when the

tension is shifted to the geometric center, the non-coincidence of the centroid of rebar layers and the beam section center induces negative bending moment at the joint interfaces.

Both local rigid rotation $\theta_r$ and chord rotation $\theta_{cr}$ are used to determine the axial force at the joint interface of S5. Regardless of the type of rotations, Fig. 16(b) illustrates that the beam axial force is not sensitive to the rotations. Even though $\theta_r$ attained around $18^o$ at the end of catenary action stage, there were no appreciable discrepancies between beam axial forces and horizontal reaction forces. Therefore, the variations of horizontal reaction forces shown in Figs. 5 to 7 can represent the variations of beam axial forces for all specimens.

Similar to the bending moment, the shear force increased first and then kept decreasing after attaining its peak value, as shown in Fig. 16(c). Unlike the axial force, after bottom bar fracture, the shear force is significantly affected by the type of rotations. At catenary action stage, the sectional shear force was solely contributed by dowel action of longitudinal bars. Therefore, a sudden reduction of the shear force followed each fracture of bottom bars. After fracture of two bottom bars, the vertical component of shear force based on the *local rigid rotation* changed from positive (i.e. up) to negative (i.e. down). The negative shear force was mainly induced by the large axial tension at the section near the joint interface not coinciding with that at the beam end. However, if evaluated based on the *chord rotation*, the shear force at the joint interface is nearly zero. This is because the axial tension throughout the beam is acting at the same beam axis, and no shear force will be induced by axial tension.

*Force transfer mechanisms at the middle joint regions*

For a deformed beam shown in Fig. 15, force equilibrium at the middle joint gives

$$P = \sum_{j=1}^{2} \left( N_j \sin\theta_j + V_j \cos\theta_j \right) \tag{1}$$

where $P$ is the applied load acting onto the middle joint (or the structural resistance), $N_j$ and $V_j$ are the axial force and the shear force transferred from beams to both joint interfaces, respectively, and $\theta_j$ is the rotation at a beam section connected to one joint interface.

Eq. (1) indicates that the vertical resistance is contributed by the vertical components of axial force and shear force throughout the beams. Fig. 17 shows the variations of each component vs. MJD. The components determined with local rigid rotation $\theta_r$ illustrate the force transfer mechanisms near the middle joint. Out of brevity, specimens S5, S7 and S8 are selected to show the decomposition of vertical resistance.

A second increase of structural resistance after CAA capacity, as shown in Figs. 17(a) and (b), was mainly caused by the vertical component of axial force changing from compression to tension. After the onset of catenary action, the contribution from axial tension increased while that from shear force decreased with increasing MJD. However, prior to bottom bar fracture, shear force still substantially contributed to structural resistance. This indicates that although *catenary action* is a tensile mechanism, structural resistance at *catenary action stage* is not solely contributed by tension. Therefore, the vertical components of axial tension cannot be simply summed as structural resistance. After fracture of bottom bars at both joint interfaces, the vertical component of shear force provided by dowel action of top bars changed direction and failed to sustain the applied load. The use of chord rotation $\theta_{cr}$ in S5 as shown in Fig. 17(a) will be discussed later.

Catenary action of S8 was mobilized at a MJD of 136 mm but failed to increase structural resistance consistently due to consecutive bar fracture, as shown in Fig. 17(c). The shear failure shown in Fig. 10(b), comprising the occurrence of a large inclined crack and the fracture of two stirrups, caused a sudden reduction of shear force at a MJD of around 100 mm, as shown in Fig. 17(c). Shear cracks damaged the compression zone near the joint interfaces, rendering S8 unable

to sustain large vertical load. As a result, the beam axial compression decreased rapidly, and catenary action had to be mobilized at a smaller displacement. This suggests that shear failure can cause early mobilization of catenary action, but catenary action might not increase structural resistance beyond CAA capacity.

*Variations of strains over reinforcing bars*

Specimen S5 is a typical example to represent the strain variations of top and bottom continuous reinforcing bars for specimens S4, S5, S7 and S8, as shown in Figs. 18(a) and (b), respectively. A bottom bar of S6 in Fig. 18(c) shows the strain variations of lap-spliced reinforcing bars used in S3 and S6. The solid lines with hollow dots denote bar strains at catenary action stage.

Based on a bending moment diagram over a beam, the beam can be divided into a positive moment (PM) region, a negative moment (NM) region and a transition region which connects these two regions. The bottom bars in the PM region (i.e. near the middle joint) and the top bars in the NM region (i.e. near the end column stub interface) were in tension throughout the entire loading process, as shown in Fig. 18. In the PM region, the bottom bars yielded in tension, followed by severe *strain concentration* at both joint interfaces, as spikes indicated in Figs. 18(b) and (c). Similarly, the strain concentration of top bars in the NM region occurred near the end column stub interface, as shown in Fig. 18(a).

In the PM region, the top bars were initially in compression and changed to tension at catenary action stage, as shown in Fig. 18(a). Due to damage of strain gages in the loading process, strain concentration of top bars at the middle joint interfaces of S5 was not visualized, but it was found in other specimens. In the NM region, the bottom bars near the end column stub interface also changed from compression to tension at catenary action stage, as shown in Figs. 18(b) and (c).

Due to large tensile strains at the joint interfaces and the end column stub interfaces, *yielding penetration* occurred inside the middle joint and the end column stubs. For example, Fig. 18(b)

shows that at a MJD of 50 mm, the bottom bar inside the middle joint has yielded. Fig. 18(a) shows that at a MJD of 74.5 mm, the top bar inside the end column stub started to yield. Yielding penetration resulted in a severe loss of bond stress and a large increment of bar slip at the interfaces, further increasing the rotation capacity of RC members.

The strains of reinforcing bars in the transition region did not vary significantly, but finally both the top and bottom bars sustained tension at catenary action stage even if the bottom bars fractured at the joint interfaces. Figs. 18(b) and (c) show that the bottom bars away from the joint interfaces for a certain distance could still contribute to axial tension force in the beam. The tension force in the bottom bars was transmitted via stirrups to the top bars, since the strain gage readings of stirrups indicate that the stirrups kept sustaining tensile force even after bottom bars fractured, as shown in Fig. 19.

**Discussions**

After the occurrence of shear failure in specimen S8, catenary action was mobilized at a relatively smaller MJD of around 136 mm, whereas catenary action commenced at around one beam depth (250 mm) for specimens S3~S7 as well as specimens S1 and S2 (Yu and Tan 2011). In other words, provided that shear failure of RC beams can be prevented, one beam depth can be regarded as the deflection corresponding to the onset of catenary action.

In practice, it is convenient to use the sum of vertical components of axial tension (i.e. $\sum_{j=1}^{2} N_j \sin\theta_j$ ) to estimate structural resistance $P$ at catenary action stage by assuming the beams to rotate as rigid bodies. That is, $\theta_j$ equals to chord rotation $\theta_{cr}$. Fig. 17(a) shows that this assumption can satisfy the equilibrium $P = 2N_{cr}\sin\theta_{cr}$ after the fracture of the bottom bars, in which $N_{cr}$ is the axial tension based on $\theta_{cr}$.

Axial tension $N_{cr}$ is affected by the bar stress and the bar fracture. Under a coupled action of shear and tension, the longitudinal bars may not fully attain the tensile strength. As shown in Fig. 5(b), the top bars fractured with a stress between the yield strength and the ultimate tensile strength. In addition, strain concentration of bars at the middle joint and end column stub interfaces may cause premature fracture. Chord rotation $\theta_{cr}$ depends on the MJD and the net span of a "single-bay" beam in a sub-assemblage. Nevertheless, it is difficult to precisely predict the MJD corresponding to bar fracture. Except specimens S5 and S8, all the other specimens attained catenary action capacity at the fracture of top bars. Note that the fracture of bottom bars at joint interfaces preceded the fracture of top bars at beam ends. Due to symmetrical reinforcement, S5 attained the capacity of catenary action when bottom bars fractured. However, for typical RC frames, the bottom reinforcement at the joint regions is less than the top reinforcement. If the allowable MJD is restricted to the value corresponding to the fracture of bottom bars, the structural resistance from catenary action will be too conservative. Table 4 shows that ultimate MJDs of specimens S3-S7 exceed 10% of total beam span length, and the corresponding structural resistances $P_{t3}$ are much higher than CAA capacities $P_{caa}$. Therefore, a simple analytical approach to predict the capacity of catenary action $P_t$ is proposed as follows:

$$P_t = 2 f_y A_{s\_top} \sin\theta_{\max} \tag{2}$$

where $f_y$ and $A_{s\_top}$ are the yield strength and the area of top bars at the middle joint interfaces, respectively; $\theta_{\max}$ is the chord rotation of beams corresponding to the MJD equal to 10% of total two-bay beam span length, i.e. 11.3°, which is also recommended in UFC 4-023-03.

It is conservative to confine steel strength to the yield strength and ignore the contribution from bottom bars, in particular, for beams with symmetrical longitudinal reinforcement, such as S5. Additionally, before taking account of catenary action, CAA capacity and maximum shear resistance should be compared to insure that no premature shear failure will occur. Otherwise,

even if catenary action is mobilized, structural resistance may not be increased further, as evidenced by the behavior of S8.

**Conclusions**

Six RC beam column sub-assemblages were quasi-statically tested under a middle column removal scenario to investigate the alternate load paths (ALPs) that can mitigate progressive collapse. The objective of the testing was to highlight structural behavior of RC sub-assemblages after the column removal. With *adequate axial and rotational restraints*, the RC sub-assemblages developed compressive arch action (CAA) and catenary action on top of flexural action. CAA capacity is 13.5%~43.2% larger than flexural action capacity calculated via conventional plastic hinge mechanism, as shown in Table 3. The capacity of catenary action is 28%~128% greater than CAA capacity for specimens S3 to S7, as shown in Table 4. However, CAA is a favorable ALP in terms of small beam deflections as catenary action requires large deformations. CAA attains its capacity at a middle joint displacement (MJD) of 0.18~0.46$h$, whereas catenary action achieve its capacity at a MJD greater than 2$h$.

Parametric study suggests that CAA can significantly increase structural resistance of the sub-assemblages with a small span-to-depth ratio and a low longitudinal reinforcement ratio, and catenary action can significantly increase structural resistance of the sub-assemblages with a large span-to-depth ratio and a high longitudinal reinforcement ratio, particularly with a high top reinforcement ratio. The detailing with symmetrical longitudinal reinforcement seems more favorable to catenary action, e.g. S5, since catenary action capacity can be attained at a smaller MJD. However, before catenary action is considered, it is necessary to compare CAA and shear capacities, in particular for a member with a short span, e.g. S8. If shear failure occurs, catenary action can be mobilized early, but it may not be able to compensate for the loss in shear. Consequently, structural resistance keeps decreasing.

Axial force throughout beams is not sensitive to beam rotations. Therefore, axial force-MJD relationships are almost the same as horizontal reaction force-MJD relationships. After the onset of catenary action, both bending moment and shear force still work over a long period at catenary action stage. Therefore, it is necessary to differentiate *catenary action* and *catenary action stage*. Catenary action is a tensile mechanism associated with the development of beam axial tension. However, at catenary action stage, catenary action is not the sole contributor to structural resistance because the vertical component of shear force also sustains vertical load. The shear force is induced by the bending moments throughout beams and is sustained by dowel action of longitudinal bars. Therefore, each fracture of longitudinal bars causes a reduction of axial tension and shear force. At catenary action stage, the contribution from beam axial tension keeps increasing whereas that from shear (or bending moments) keeps decreasing. Whether catenary action can increase structural resistance depends on whether the contribution of beam axial tension can exceed the loss in shear.

Failure modes of the specimens and strain gage readings of the reinforcing bars indicate that all specimens failed at the middle joint interfaces and the end column stub interfaces. Prior to bar fracture, severe strain concentration occurred at these interfaces. Therefore, if high catenary action capacity is expected at a relatively smaller deflection during structure design, measures should be taken to reduce local strain concentration.

## Acknowledgement

The authors gratefully acknowledge the research funding provided by Defence Science & Technology Agency, Singapore.

## References


American Concrete Institute. (2004). *ACI SP-66(04): ACI Detailing Manual*, Farmington Hills.

American Concrete Institute. (2005). "ACI 318-05: Building Code Requirements for Structural Concrete." Farmington Hills,, Michigan.

American Society of Civil Engineers (ASCE). (2005). "Minimum Design Loads for Buildings and Other Structures." American Society of Civil Engineers, Reston, Virginia.

Department of Defense (DOD). (2010). "Design of Buildings to Resist Progressive Collapse." Unified Facilities Criteria (UFC) 4-023-03, 27 January, 2010.

Ellingwood, B., and Leyendecker, E. V. (1978). "Approaches for design against progressive collapse." *Journal of the Structural Division, ASCE*, 18(ST3), 413-423.

European Committee for Standardization. (2006). "EN 1991-2-7: Eurocode 1 - Actions on structures - Part 1-7: General actions - Accidental actions." CEN, Brussels.

General Services Administration (GSA). (2003). "Progressive Collapse Analysis and Design Guidelines for New Federal Office Buildings and Major Modernization Projects."

Gurley, C. R. (2008). "Progressive Collapse and Earthquake Resistance." *Practice Periodical on Structural Design and Construction*, 13(1), 19-23.

Orton, S., Jirsa, J., and Bayrak, O. (2009). "Carbon Fiber-Reinforced Polymer for Continuity in Existing Reinforced Cocnrete Buildings Vulnerable to Collapse." *ACI Structural Journal*, 106(5), 608-616.

Park, R., and Gamble, W. L. (2000). *Reinforced Concrete Slabs*, John Wiley & Sons, Inc.

Sasani, M., Bazan, M., and Sagiroglu, S. (2007). "Experimental and analytical progressive collapse evaluation of actual reinforced concrete structure." *ACI Structural Journal*, 104(6), 731-739.

Sasani, M., Kazemi, A., Sagiroglu, S., and Forest, S. (2011). "Progressive Collapse Resistance of an Actual 11-Story Structure Subjected to Severe Initial Damage." *Journal of Structural Engineering*, 137(9), 893.

Sasani, M., and Kropelnicki, J. (2008). "Progressive collapse analysis of an RC structure." *The Structural Design of Tall and Special Buildings*, 17(4), 757-771.

Su, Y., P., Tian, Y., and Song, X. S. (2009). "Progressive collapse resistance of axially-restrained frame beams." *ACI Structural Journal*, 106(5), 600-607.

Yi, W. J., He, Q. F., Xiao, Y., and Kunnath, S. K. (2008). "Experimental study on progressive collapse-resistant behavior of reinforced concrete frame structures." *ACI Structural Journal*, 105(4), 433-439.

Yu, J., and Tan, K. H. (2010a). "Experimental study on catenary action of RC beam-column sub-assemblages." *The Third International fib Congress and Exhibition*, Gaylord National Resort, Washington,D.C., Paper #205 in Proceedings Disc.

Yu, J., and Tan, K. H. (2010b). "Progressive collapse resistance of RC beam-column sub-assemblages." *Design and Analysis of Protective Structures 2010*, Singapore, 74-83.

Yu, J., and Tan, K. H. (2011). "Experimental and numerical investigation on progressive collapse resistance of reinforced concrete beam column sub-assemblages." *Engineering Structures* (online).

## Figure list

**Table list:**

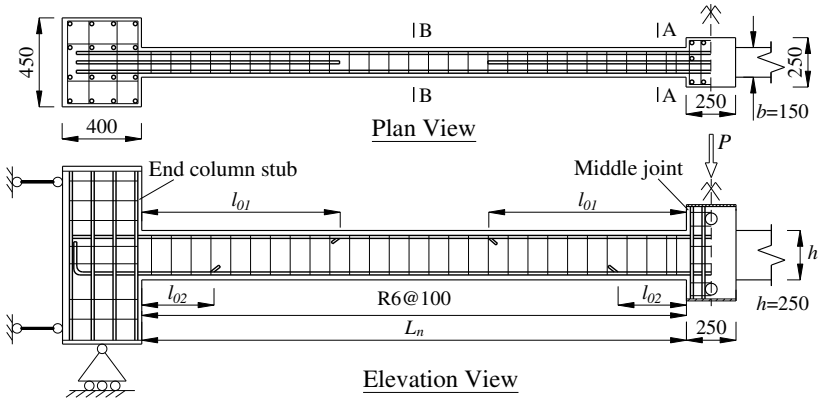


**Fig. 1: Detailing and boundary conditions of specimens (Unit: mm)**

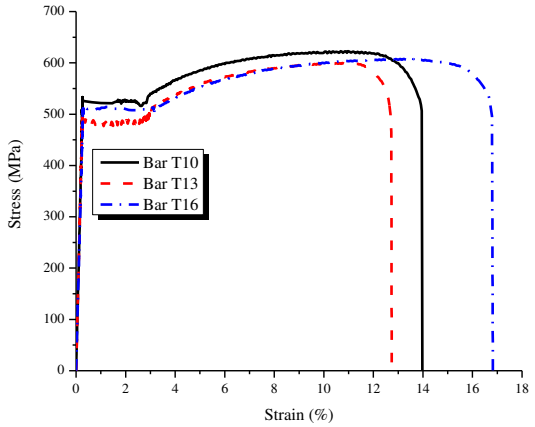


**Fig. 2: Stress-strain relationships of reinforcing bars**

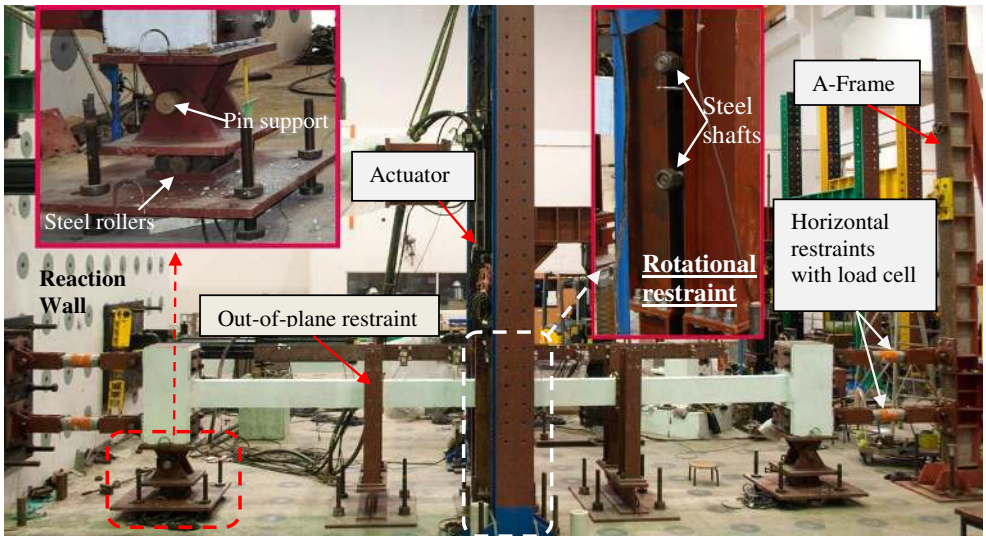


**Fig. 3: Test set-up**

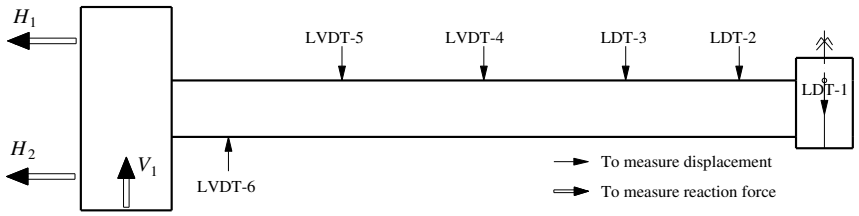


**Fig. 4: Arrangement of instrumentation**

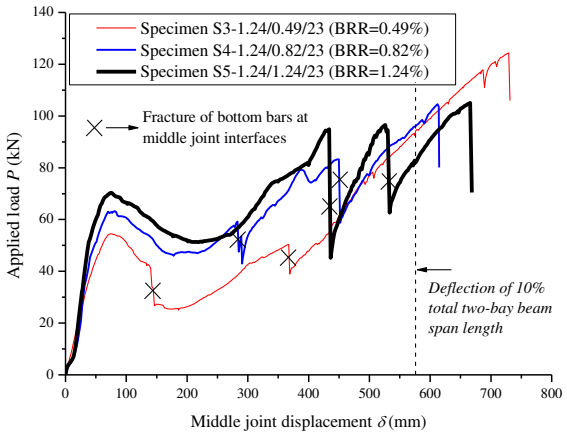


(a)

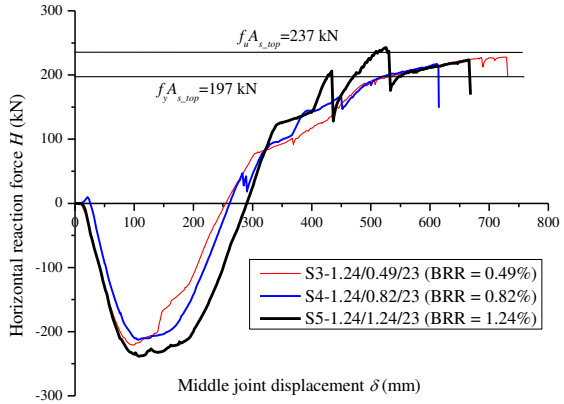


(b)

**Fig. 5: Effect of bottom reinforcement ratio at middle joints on structural behavior of sub-assemblages: (a) Load-MJD relationship; (b) Horizontal reaction force-MJD relationship ($A_{s\_top}$: area of top reinforcement at joint interfaces)**

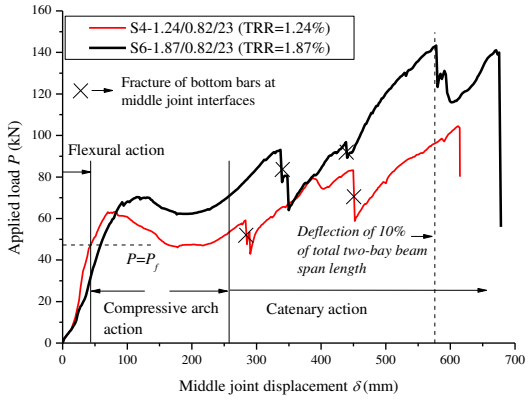


(a) Load-MJD relationship

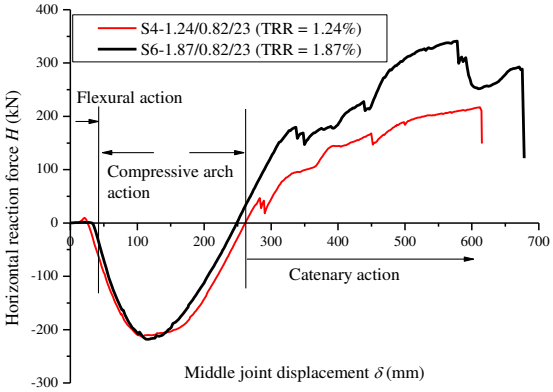


(b) Horizontal reaction force-MJD relationship

**Fig. 6: Effect of top reinforcement ratio at middle joints on structural behavior of sub-assemblages**

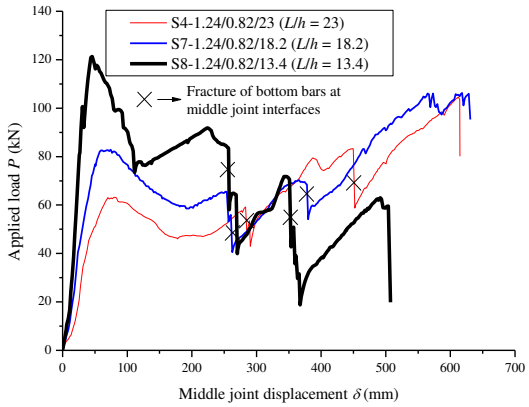


(a) Load-MJD relationship

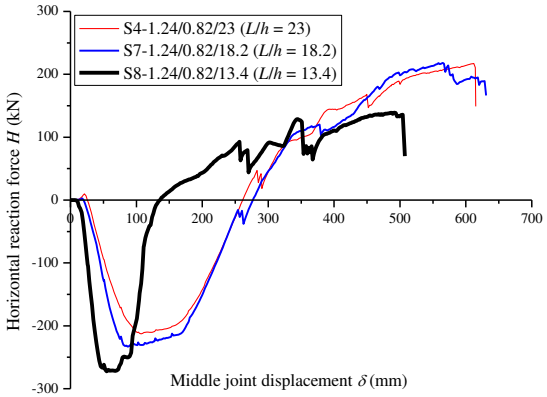


(b) Horizontal reaction force-MJD relationship

**Fig. 7: Effect of beam span-to-depth ratio on structural behavior of sub-assemblages**

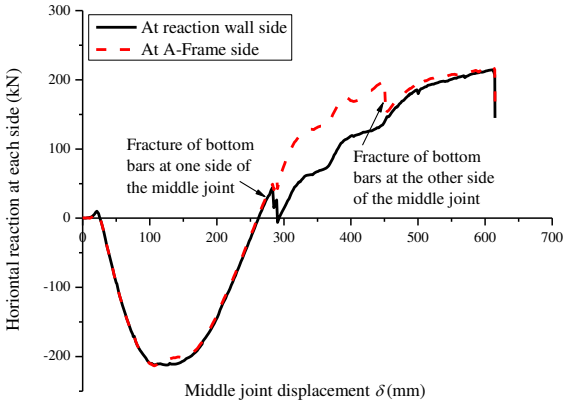


(a) Specimen S4

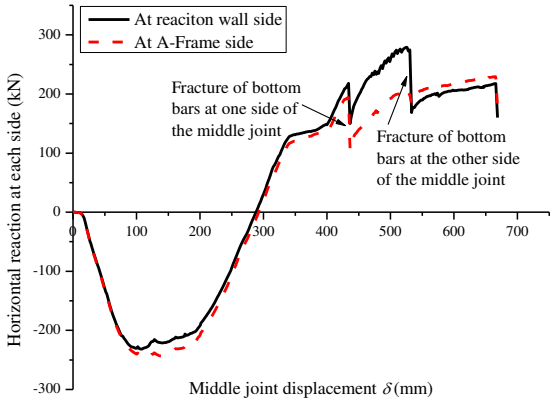


(b) Specimen S5

**Fig. 8: Development of horizontal reaction at each end of a specimen**

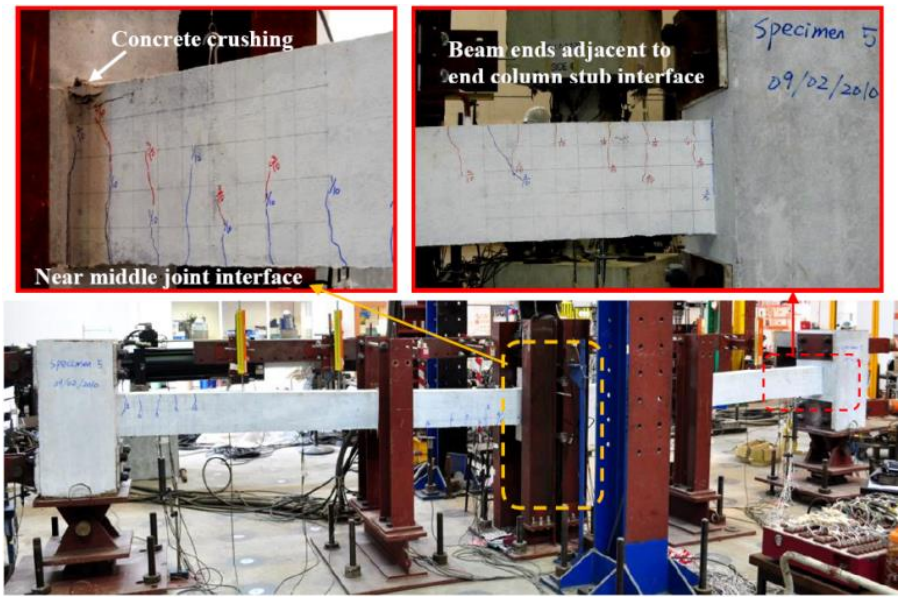


(a) At the capacity of CAA ($\delta$=75 mm)

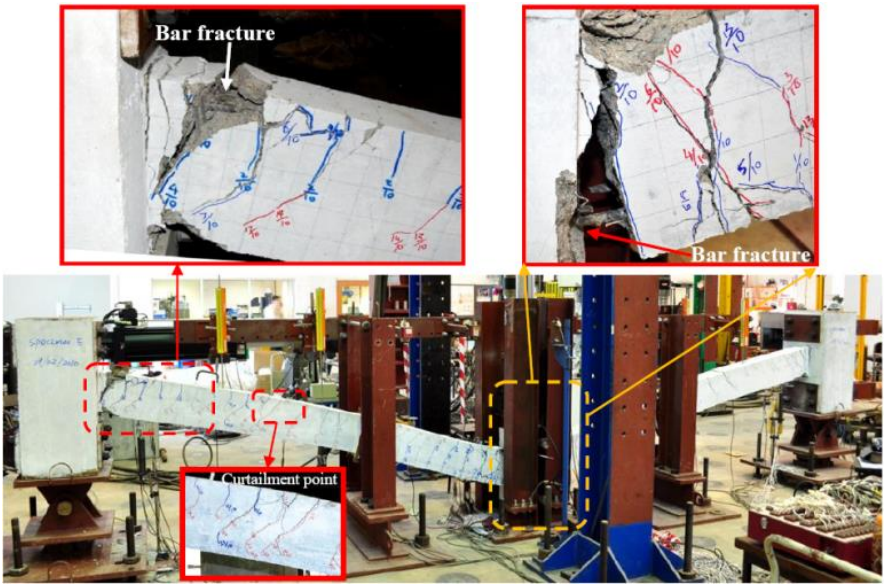


(b) At the capacity of catenary action ($\delta$=665 mm)

**Fig. 9: Failure modes and crack patterns of specimen S5**

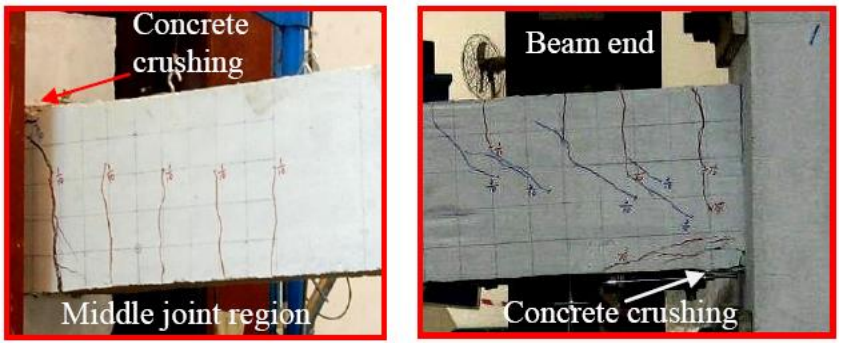


(a) At CAA stage ($\delta$=75 mm)

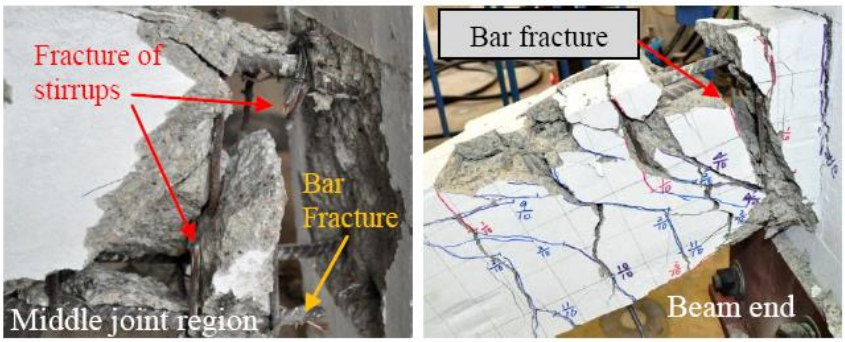


(b) At catenary action capacity ($\delta$=504 mm)

**Fig. 10: Failure modes and crack patterns of specimen S8**

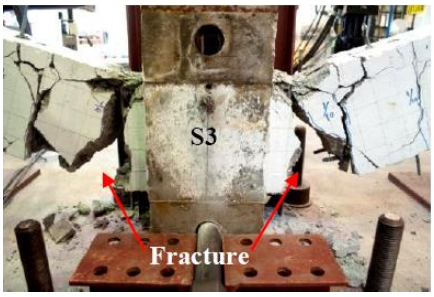


(a) S3-1.24/0.49/23 (lap-spliced bottom bars)


(b) S4-1.24/0.82/23 (continuous bottom bars)


(c) S5-1.24/1.24/23 (continuous bottom bars)

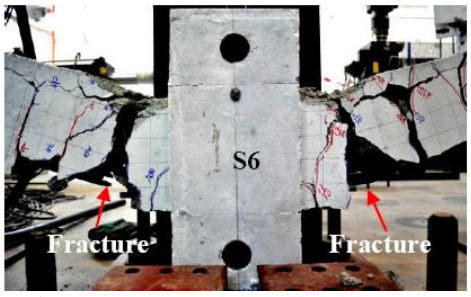


(d) S6-1.87/0.82/23 (lap-spliced bottom bars)

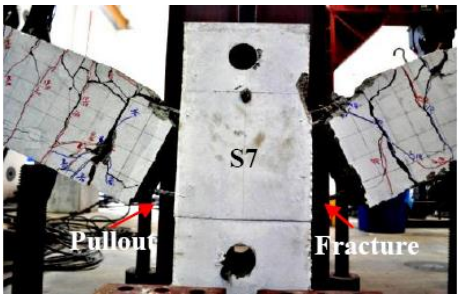


(e) S7-1.24/0.82/18.2 (continuous bottom bars)

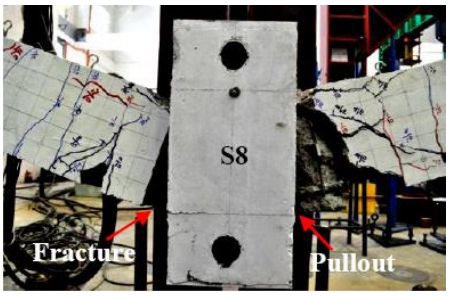


(f) S8-1.24/0.82/13.4 (continuous bottom bars)

**Fig. 11: Local failure modes at middle joint regions**

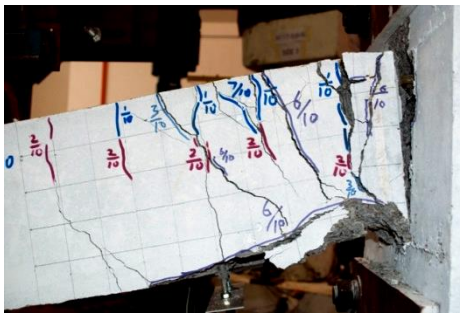

(a) S3-1.24/0.49/23

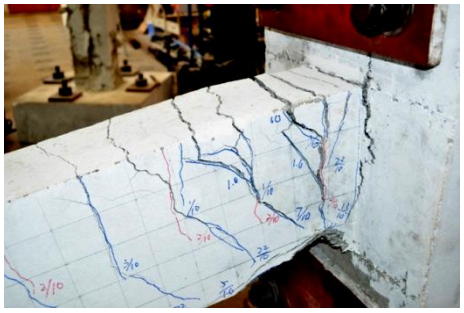

(b) S4-1.24/0.82/23

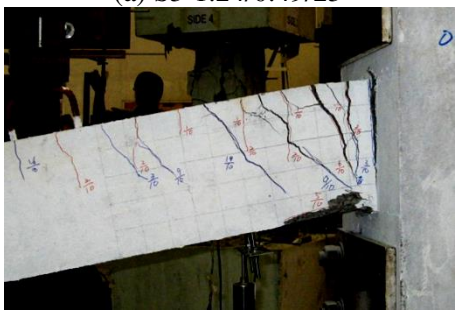

(c) S5-1.24/1.24/23

(d) S6-1.87/0.82/23

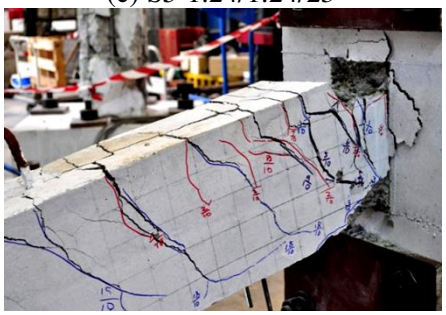

(e) S7-1.24/0.82/18.2

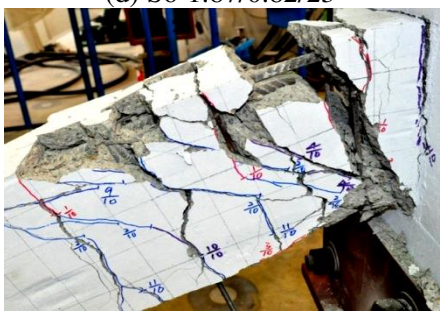

(f) S8-1.24/0.82/13.4

**Fig. 12: Local failure modes at beam ends**

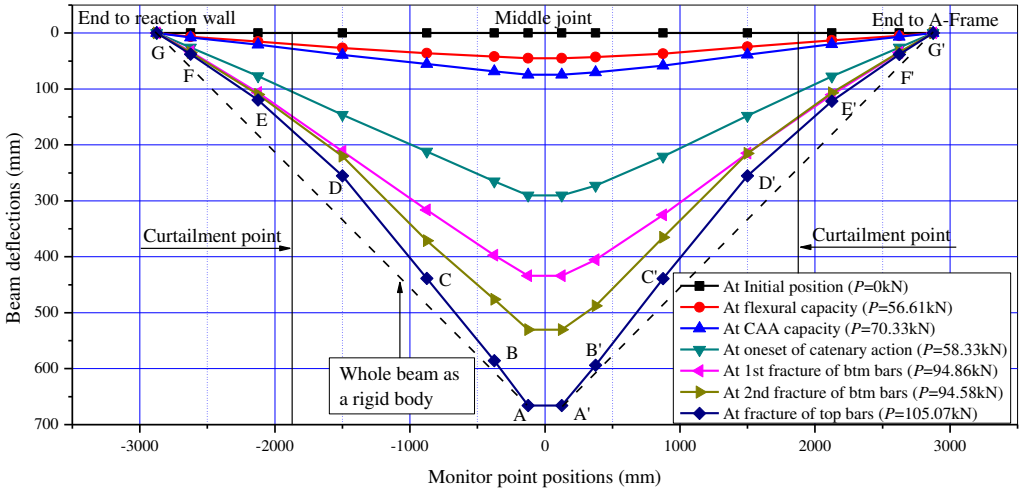


**Fig. 13: Overall deflection curves of specimen S5**

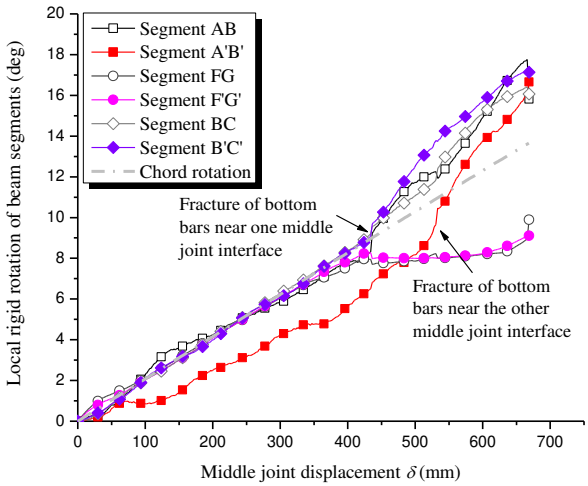


**Fig. 14: Development of local and chord rotation of specimen S5**

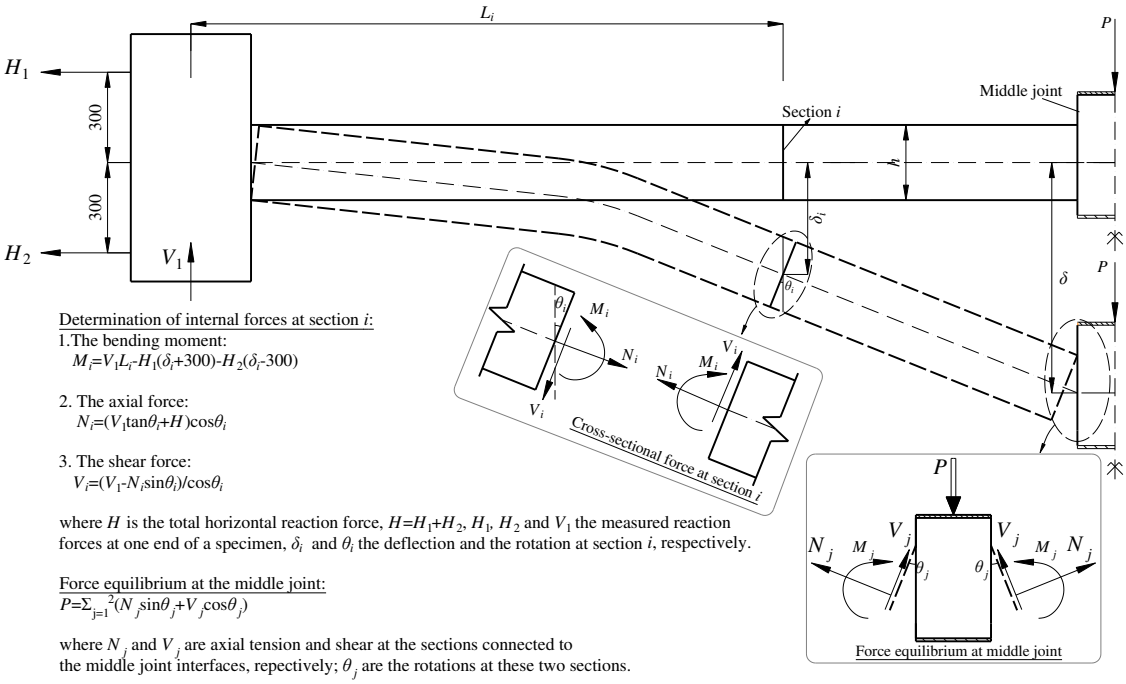


Determination of internal forces at section *i*:

1.The bending moment:

$M_i=V_1L_i-H_1(\delta_i+300)-H_2(\delta_i-300)$

2. The axial force:

$N_i=(V_1\tan\theta_i+H)\cos\theta_i$

3. The shear force:

$V_i=(V_1-N_i\sin\theta_i)/\cos\theta_i$

where $H$ is the total horizontal reaction force, $H=H_1+H_2$, $H_1$, $H_2$ and $V_1$ the measured reaction forces at one end of a specimen, $\delta_i$ and $\theta_i$ the deflection and the rotation at section *i*, respectively.

Force equilibrium at the middle joint:

$P=\Sigma_{j=1}^{2}(N_j\sin\theta_j+V_j\cos\theta_j)$

where $N_j$ and $V_j$ are axial tension and shear at the sections connected to the middle joint interfaces, repectively; $\theta_j$ are the rotations at these two sections.

**Fig. 15: Determination of internal forces**

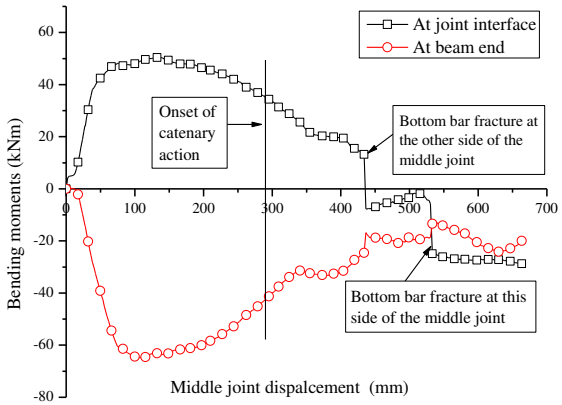


(a) Variation of bending moment

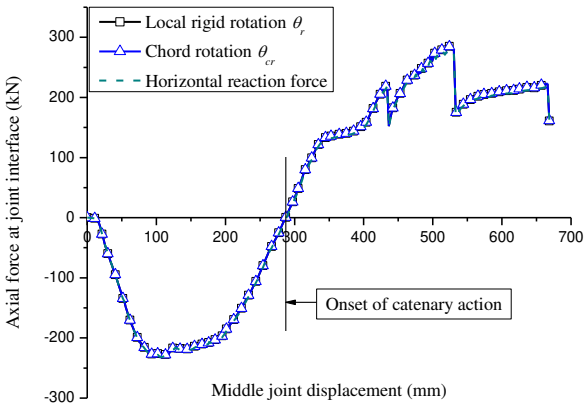


(b) Axial force at the beam section connected to the joint interface

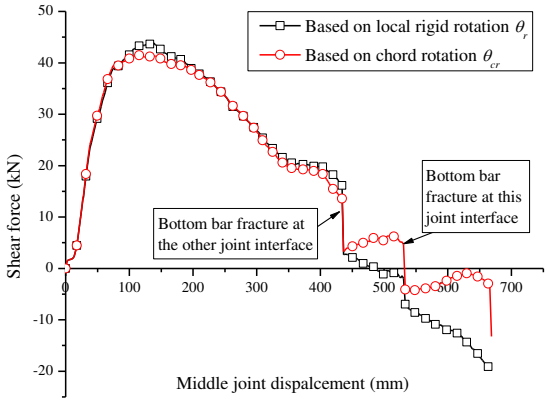


(c) Shear force at the beam section connected to the joint interface

**Fig. 16: Variations of cross-sectional forces of specimen S5**

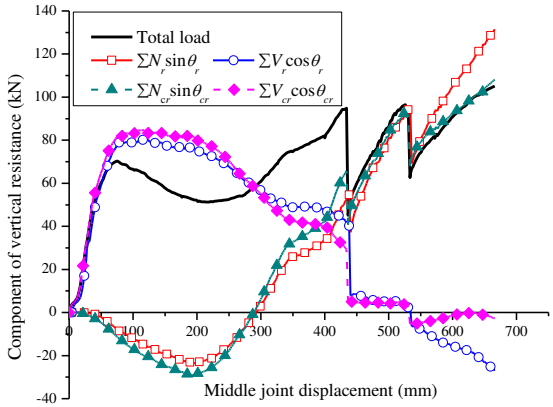


(a) Specimen S5

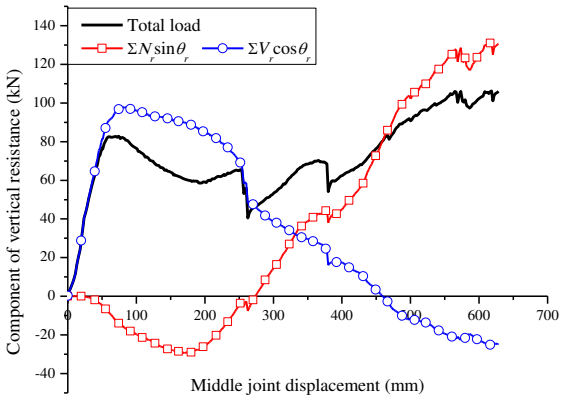


(b) Specimen S7

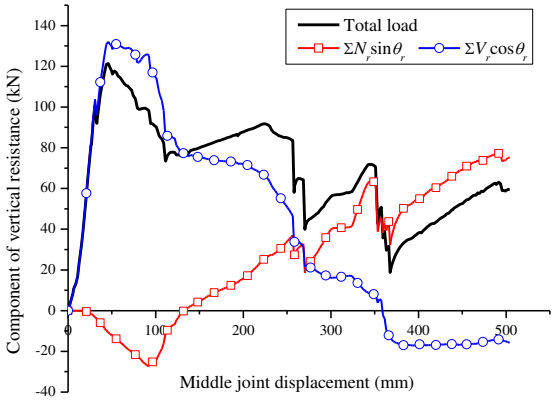


(c) Specimen S8

**Fig. 17: Decomposition of vertical resistance**

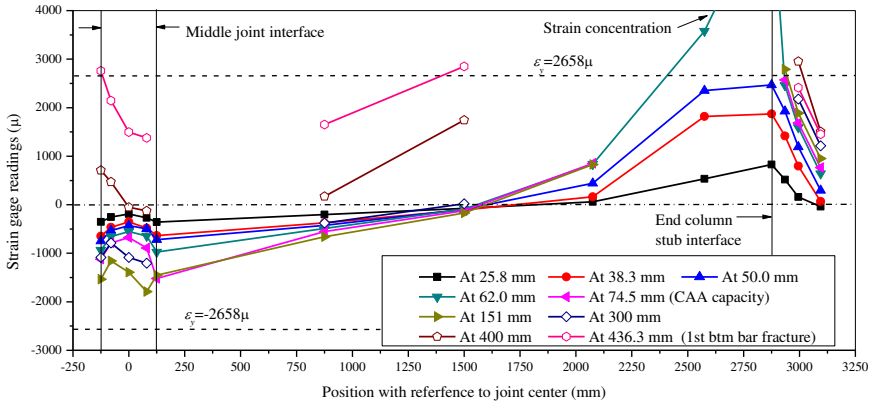


(a) Top reinforcement in S5

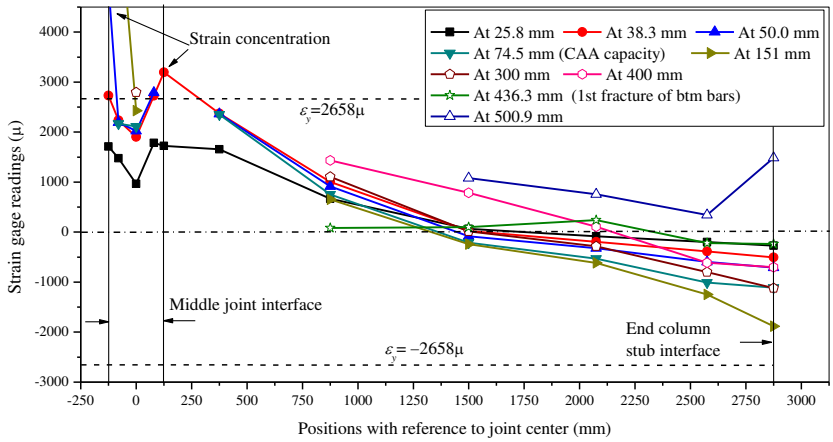


(b) Bottom reinforcement in S5

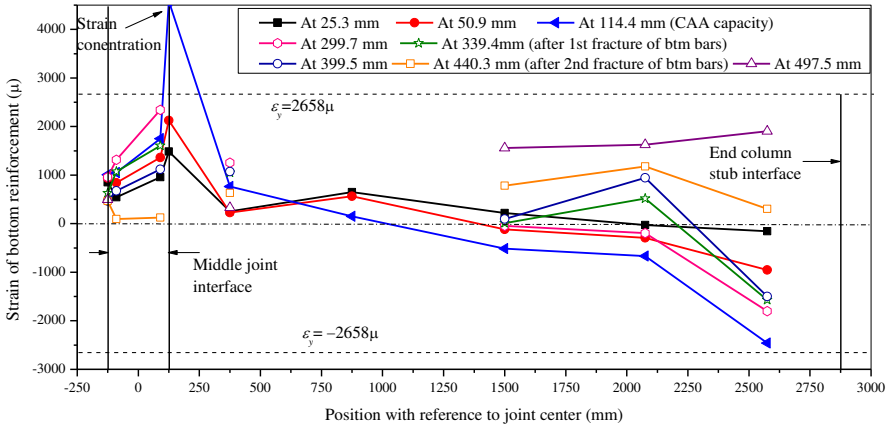


(c) Bottom reinforcement along S6

**Fig. 18: Variations of longitudinal reinforcement strains**

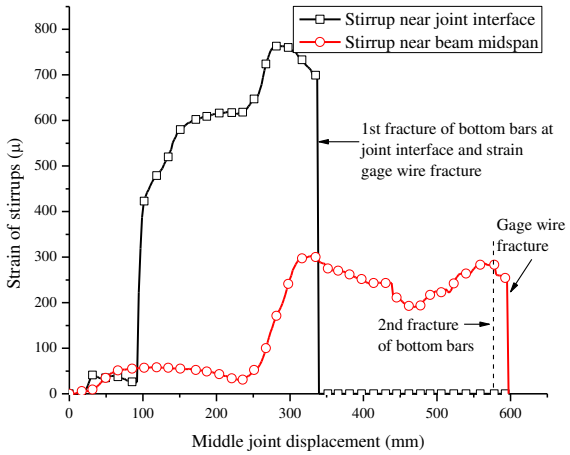


**Fig. 19 Strains of stirrups in Specimen S6**

**Table 1: Geometric properties of sub-assemblage specimens***

| Test | $L_n$ (mm) | $L/h$ | Position of curtailment (mm) | | Longitudinal reinforcement‡ | | | | Bottom bars at middle joints§ |
|---|---|---|---|---|---|---|---|---|---|
| | | | | | A-A section | | B-B section | | |
| | | | $l_{01}$ | $l_{02}$ | Top | Bottom | Top | Bottom | |
| S1-0.90/0.49/23S† | 2750 | 23 | 1000 | N/A | 1T13 +2T10 (0.90%) | 2T10 (0.49%) | 2T10 (0.49%) | 2T10 (0.49%) | continuous |
| S2-0.73/0.49/23 | 2750 | 23 | 925 | N/A | 3T10 (0.73%) | 2T10 (0.49%) | 2T10 (0.49%) | 2T10 (0.49%) | lap-splice |
| S3-1.24/0.49/23 | 2750 | 23 | 1000 | 345 | 3T13 (1.24%) | 2T10 (0.49%) | 2T13 (0.82%) | 2T10 +1T13 (0.90%) | lap-splice |
| S4-1.24/0.82/23 | 2750 | 23 | 1000 | N/A | 3T13 (1.24%) | 2T13 (0.82%) | 2T13 (0.82%) | 2T13 (0.82%) | continuous |
| S5-1.24/1.24/23 | 2750 | 23 | 1000 | N/A | 3T13 (1.24%) | 3T13 (1.24%) | 2T13 (0.82%) | 3T13 (1.24%) | continuous |
| S6-1.87/0.82/23 | 2750 | 23 | 1000 | 345 | 3T16 (1.87%) | 2T13 (0.82%) | 2T16 (1.25%) | 2T13 (0.82%) | continuous |
| S7-1.24/0.82/18.2 | 2150 | 18.2 | 780 | N/A | 3T13 (1.24%) | 2T13 (0.82%) | 2T13 (0.82%) | 2T13 (0.82%) | continuous |
| S8-1.24/0.82/13.4 | 1550 | 13.4 | 560 | N/A | 3T13 (1.24%) | 2T13 (0.82%) | 2T13 (0.82%) | 2T13 (0.82%) | continuous |

*: The beam sections are 150 mm wide and 250 mm deep for all specimens, i.e. $b$ = 150 mm and $h$ =250 mm; The concrete cover thickness was 20 mm for all specimens; total net span $\boldsymbol{L=2L_n+250}$ (mm); Test results of S1 and S2 are shown in paper (Yu and Tan 2011)

†: "S" indicates seismic detailing in terms of arrangement of stirrups.

‡: Reinforcement ratio in brackets is calculated by $A_s / bd$ , where $b$=150 mm and $d$=215 mm; A-A and B-B sections are referred to Fig. 1.

§: the lap splice lengths for bottom bars of specimen S3 and S6 are 410 mm and 530 mm, respectively. The lap-spliced position is through the middle joint.

**Table 2: Material properties of steel reinforcement**

| Bar type* | Yield strength $f_y$ (MPa) | Elastic Modulus $E_s$ (MPa) | Strain at the start of hardening $\varepsilon_{sh}$ (%) | Tensile strength $f_u$ (MPa) | Ultimate strain $\varepsilon_u$ (%) |
|---|---|---|---|---|---|
| R6 | 349 | 199177 | -- | 459 | -- |
| T10 | 511 | 211020 | 2.51 | 622 | 11.00 |
| T13 | 494 | 185873 | 2.66 | 593 | 10.92 |
| T16 | 513 | 184423 | 2.87 | 612 | 13.43 |

*:"R" and "T" denote low-yield and high-yield strength reinforcement, with a nominal yield strength of 250 MPa and 460 MPa, respectively; The numeral after "R" or "T" represents the nominal diameter of a bar.

**Table 3: Experimental results at flexural and CAA stage**

| Specimen | Flexural action | Compressive arch action (CAA) | | | | | |
|---|---|---|---|---|---|---|---|
| | Calculated capacity $P_f$ * (kN) | Peak load $P_{caa}$ † (kN) | MJD at $P_{caa}$ (mm) | Horizontal reaction at $P_{caa}$ (kN) | Max. compressive horizontal reaction $N_{max}$ (kN) | MJD at $N_{max}$ (mm) | Enhancement factor $\alpha$ (%)‡ |
| S1 | 33.08 | 41.64 | 78 | -165.3 | 177.90 | 114.3 | 25.9 |
| S2 | 29.02 | 38.38 | 73 | -145.7 | 155.90 | 128.3 | 32.2 |
| S3 | 40.89 | 54.47 | 74.4 | -196.40 | 221.00 | 100.1 | 33.2 |
| S4 | 47.76 | 63.22 | 81.0 | -183.10 | 212.65 | 107.2 | 32.4 |
| S5 | 56.61 | 70.33 | 74.5 | -207.00 | 238.35 | 108.7 | 24.2 |
| S6 | 61.97 | 70.33 | 114.4 | -218.10 | 218.10 | 114.4 | 13.5 |
| S7 | 61.09 | 82.82 | 74.4 | -220.00 | 233.10 | 87.0 | 35.6 |
| S8 | 84.74 | 121.34 | 45.9 | -264.50 | 272.50 | 55.0 | 43.2 |

*: $P_f$ is calculated based on conventional plastic hinge mechanism;

†: $P_{caa}$ corresponds to the first peak load in the load-MJD curves, named as CAA capacity.

‡: Enhancement factor $\alpha = \left(P_{caa} - P_f\right) / P_f$ .

**Table 4: Experimental results at catenary action stage**

| Specimen | MJD at the start of catenary action (mm) | Load at 1st fracture of bottom bars $P_{t1}$ (kN) | MJD at $P_{t1}$ (mm) | Load at 2nd fracture of bottom bars $P_{t2}$ (kN) | MJD at $P_{t2}$ (mm) | Load at fracture of top bars $P_{t3}^{*}$ (kN) | MJD at $P_{t3}$ (mm) | $\frac{P_{t3}}{P_{caa}}$ † |
|---|---|---|---|---|---|---|---|---|
| S1 | 307.1 | 25.91 | 227.0 | -- | -- | 68.91 | 573.0 | 1.65 |
| S2 | 294.4 | 39.1 | 378.7 | -- | -- | 67.63 | 612.0 | 1.76 |
| S3 | 254.1 | 41.26 | 140.1 | 50.35 | 367.2 | 124.37 | 729.3 | 2.28 |
| S4 | 261.6 | 59.18 | 283.0 | 83.24 | 449.6 | 103.68 | 614.3 | 1.64 |
| S5 | 290.3 | 94.86 | 433.9 | 94.58 | 530.3 | 105.07 | 665.9 | 1.49 |
| S6 | 248.7 | 93.03 | 337.1 | 96.82 | 438.4 | 139.90 | 675.3 | 1.99 |
| S7 | 276.7 | 65.43 | 254.1 | 68.43 | 378.2 | 105.99 | 628.5 | 1.28 |
| S8 | 136.0 | 83.53 | 256.6 | 70.62 | 351.0 | 59.58 | 504.1 | 0.49 |

*: Except for S6 and S8, $P_{t3}$ of the other specimens represents the capacity of catenary action; catenary action capacities of S6 and S8 are 143.28 kN and 91.83 kN, respectively;

†: $P_{caa}$ denotes structural capacity of compressive arch action

**Table 5: Ultimate rotations at joint interfaces and at beam ends**

| Test | Local rigid rotation at joint interfaces (deg) | | Local rigid rotation at beam ends (deg) | | Chord rotation* (deg) |
|---|---|---|---|---|---|
| | A-Frame side | Reaction Wall side | A-Frame side | Reaction Wall side | |
| S3 | 20.9 | 23.1 | 9.8 | 8.4 | 14.9 |
| S4 | 15.0 | 15.7 | 7.4 | 6.6 | 12.6 |
| S5 | 16.0 | 17.8 | 8.7 | 8.6 | 13.6 |
| S6 | 22.0 | 19.2 | 10.6 | 8.4 | 13.8 |
| S7 | 17.7 | 21.7 | 11.6 | 9.3 | 16.3 |
| S8 | 17.7 | 13.9 | 17.5 | 13.9 | 18.0 |

*: The ultimate chord rotation of each specimen is achieved after the fracture of boom bars near the middle joint interfaces and just before the complete fracture of top bars at one beam end.